# Exploring the potential of the novel imidazole-4,5-dicarboxyamide chemical exchange saturation transfer scaffold for pH and perfusion imaging

**Shaowei Bo**[1,†], **Julia Stabinska**[1,3], **Yunkou Wu**[1], **KowsalyaDevi Pavuluri**[1,‡], **Aruna Singh**[1,3], **Zinia Mohanta**[1,3], **Rehan Choudhry**[1], **Max Kates**[2], **Farzad Sedaghat**[1], **Zaver Bhujwalla**[1], **Martin G. Pomper**[1,2], **Michael T. McMahon**[*,1,3]

[1]The Russell H. Morgan Department of Radiology and Radiological Science, The Johns Hopkins University School of Medicine, Baltimore, MD.

[2]The James Buchanan Brady Urological Institute and Department of Urology, Johns Hopkins University School of Medicine, Baltimore, MD.

[3]F.M. Kirby Research Center for Functional Brain Imaging, Kennedy Krieger Institute, Baltimore, MD.

## Abstract

Here we describe and assess the potential of 14 newly synthesized imidazole-4,5-dicarboxyamides (**I45DCs**) for pH and perfusion imaging. A number of these aromatic compounds possess large labile proton chemical shifts (up to 7.7 ppm from water) due to their intramolecular hydrogen bonds and a second labile proton to allow for CEST signal ratio based pH measurements. We have found that the contrast produced is strong for a wide range of substitutions and that the inflection points in the CEST signal ratios vs pH plots used to generate concentration independent pH maps can be adjusted based on these subsitutions to tune the pH range that can be measured. These **I45DC** CEST agents have advantages over the triiodobenzenes currently being employed for tumor and kidney pH mapping both preclinically and in intial human studies. Finally, as CEST MRI combined with exogenous contrast has the potential to detect functional changes in the kidneys, we evaluated our highest performing anionic compound (**I45DC-diGlu**) on a unilateral urinary obstruction mouse model and observed lower contrast uptake in the obstructed kidney compared to the unobstructed kidney and that the unobstructed kidney displayed a pH ~ 6.5 while the obstructed kidney had elevated pH and increased range in pH values. Based on this, we conclude that the **I45DCs** have excellent imaging properties and hold promise for a variety of medical imaging applications, particularly renal imaging.

## Graphical Abstract

*\*Corresponding Author* Michael T. McMahon, Ph. D., Address: F.M. Kirby Research Center for Functional Brain Imaging, Kennedy Krieger Institute, 707 N. Broadway Ave., Baltimore, Maryland 21205, mcmahon@kennedykrieger.org, Telephone: 443-923-9356.
†Department of Medical Imaging Center, The First Affiliated Hospital of Jinan University, Jinan University, Guangzhou 510630, China.
‡Department of Radiology, Mayo Clinic, Rochester, Minnesota, United States.

This manuscript describes the synthesis and characterization of a novel series of CEST MRI pH imaging agents based on imidazoles and testing the top agent on a Unilateral Urinary Obstruction mouse model.

## Keywords

CEST MRI; imidazoles; functional kidney imaging; contrast agents

## 1 | INTRODUCTION

Chemical exchange saturation transfer (CEST) MRI is an emerging MRI technique that involves selective saturation of labile protons (including hydroxyl (-OH), amide (-CONH), amine ($-NH_2$) and thiol (-SH) proton) on the molecules, followed by rapid saturation transfer between various labile protons and the bulk water pool[1-6]. This process allows signal amplifications of factors of 500 or more to allow detection of low concentrations of CEST agents[5]. Another feature of CEST contrast is that the exchange rate is related to environmental pH, and clever design of CEST probes can be used to produce pH maps through looking at the ratio of two signals at different frequencies[7-9]. This contrast can be produced both by endogenous compounds, which has been tested for providing additional diagnostic information for tumor patients[10,11] and exogenously administered compounds such as glucose in the first patient evaluations for highlighting tumors[12,13]. However, most organic CEST agents suffer from reduced sensitivity at 3 T and below because of low SNR, shorter endogenous T1, and insufficient exchangeable proton chemical shift from water for detection at these clinical field strengths. Therefore, there is an emerging need to identify new high performance and well tolerated CEST agents.

Obstructive uropathy is a type of kidney injury based on impaired urine transit most commonly occurring due to obstructing stones, strictures, malignancy or congenital anatomic causes. While the relationship between urinary obstruction and acute kidney injury (AKI) is well established, a recent multicenter investigation revealed an independent association with chronic kidney disease (CKD), resulting in increased patient morbidity and mortality[14]. Despite the risk of irreversible renal injury, current laboratory and diagnostic techniques remain limited in assessing renal injury in the setting of urinary obstruction (especially in the setting of confounding comorbidities like diabetes and hypertension), which may lead to delayed intervention and permanent kidney damage. Standard blood and urine tests are not very informative about the extent of renal injury and the reversibility of renal impairment for UTO patients[15]. Multi-phase computed tomography is often utilized to assess the etiology of a urinary obstruction, but is unable to fully quantify loss in kidney function. Renal scintigraphy allows measurement of differential function but presents challenges due to its low resolution, challenges with handling motion and limits for performing after hours or on offsite patients[16,17]. In this context, kidney tissue pH could provide more information on kidney function, particularly for patients with UTOs, because the kidneys are one of the main controllers of acid-base equilibrium and aberrations in renal parenchymal pH may be an indicator of incipient renal injury. Moreover, in the setting of nephrolithiasis, urine pH tests are widely utilized, as deviations in urine pH

can predispose to stone formation. There are several MRI strategies for measuring pH including use of spectroscopic pH imaging probes such as ISUCA[18], use of pH dependent relaxation probes[19,20] and use of hyperpolarized bicarbonate[21]. Recently PET/MRI was used to measure in vivo tumor pHe with PET/MRI co-agents, which showed great promise in clinical translation [22]. However, all of these methods have limitations for translating to patients, for spectroscopic imaging probes there are sensitivity limitations, for relaxation probe pH mapping of the kidneys there are challenges due to difficulties teasing out changes in concentration from changes in pH and for hyperpolarized probes there are limitations imposed by the length of time that the polarization remains based on relaxation, for PET/MRI there are limitations imposed by requiring to perform both PET and MR and co-register these images. A method which can more readily separate these changes out with good sensitivity and no time limitations could render MRI based pH imaging as a good diagnostic for kidney imaging, particularly for managing UTO patients.

Based on the potential of CEST imaging for pH maps, we have long been interested in preparing CEST probes that are well suited for pH measurements. In order to get around the sensitivity limitations of CEST imaging, we and others have sought out and found special aromatic compounds with large labile proton chemical shifts (> 5.0 ppm) and suitable proton exchange rates based on the tuning of these two properties through intramolecular hydrogen bond including the salicylates, anthranilates, porphyrins, hydrazones and acetanilides[23-28]. Previously, we have identified two Imidazole- 4,5-dicarboxyamides (**I45DCs**) which were well tolerated, possessing -NH protons resonating 7.7 – 7.8 ppm upfield from water and also with two labile protons to enable producing ratiometric pH maps, **I45DC-diGlu** and **I45DC-diAsp**[29]. In the present study, we have explored the potential of an extended series of **I45DCs** including synthesizing 14 new **I45DCs** and testing them in vitro for their CEST MRI properties in the physiological pH range. Our most promising agent (**I45DC-diGlu**) was then tested in vivo on a unilateral urinary obstruction (UUO) mouse model of UTO to determine if administration of this compound could detect differences between obstructed and unobstructed kidneys.

## 2 | MATERIALS AND METHODS

### 2.1 General Chemistry

Unless otherwise specified, the syntheses described below were carried out at ambient atmosphere and temperature. Anhydrous solvents such as N,N-Dimethylformamide (DMF), diisopropylethylamine (DIPEA) and benzene were purchased from Sigma-Aldrich. The solvent $H_2O$ was obtained from a purification system from EMD Millipore. Deuterated solvents were purchased from Cambridge Isotope Laboratories. All other reagents and solvents were purchased from commercial vendors and used without further purification. HPLC purifications were performed using $^{12}C$ columns (20 mm × 250 mm, Phenomenex Inc.) at 6 mL/min flow rate of water-acetonitrile eluent, unless otherwise specified. $^1H$ NMR spectra were recorded on a 500 MHz spectrometer. The chemical shifts are reported as δ values (ppm) relative to the water signal in deuterated methanol (MeOD). Mass spectral analyses were performed using the electrospray ionization (ESI) method.

## 2.2 Synthesis of imidazole-4,5-dicarboxamides

To a dry round-bottom flask **I45DCA** (3.12 g, 20.0 mmol) and 30 mL of benzene were added. To this stirred suspension 13.0 mL of thionyl chloride (180.0 mmol) and 0.772 mL of DMF (10.0 mmol) were added and the resulting mixture was refluxed for 16 h. After the mixture was cooled to room temperature, the solid product was collected by vacuum filtration, washed with two 20 mL portions of benzene, and dried under vacuum to yield **acyl chloride**, which was used without characterization. Then to a suspension of **acyl chloride** (**1**, 1.56 g, 5.0 mmol) and *N,N*-diethylaniline (1.60 mL, 10 mmol) in THF (30 mL), **H-Glu(OtBu)-OtBu·HCl** (2.96 g, 10.0 mmol) were added at −78±C. The reaction was kept for 1 hr at this temperature and then warmed to room temperature. After stirring 3 h, the yellow solid was precipitated from the solvent and filtered to give **Glu-Pyrazine** in 90% yield. Then to a stirring solution of **Glu-Pyrazine** (379 mg, 0.5 mmol) and **H-Thr-OtBu·HCl** (423.0 mg, 2.0 mmol) in THF (30 mL) DIPEA (517 mg, 4.0 mmol) was added. After stirring for 6h, the solvent was evaporated and crude product was purified by flash column chromatography to get the intermediate. This intermediate was dissolved in 5 mL TFA/DCM (1/1) for 2 h at room temperature. After all of the solvent was removed under vacuum, **I45DC-GluThr** was purified by HPLC. Compounds **GluTyr**, **GluTrp**, **GluArg**, **GluLys**, **GluLeu**, **GluEa**, **diGlu**, and **GluTrp** were synthesized with a similar procedure (Scheme 1).

**GluTyr** yield 55% white powder. LCMS ESI$^+$: 471.14 [M+Na], expected mass for $C_{19}H_{20}N_4NaO_9^+$ 471.11. $^1$H NMR (500 MHz, MeOD): δ 7.74 (s, 1H), 7.07 (d, *J*=10.0 Hz, 2H), 6.67 (d, *J*=10.0 Hz, 2H), 4.77-4.80 (m, 1H), 4.66-4.69 (m, 1H), 3.19-3.23 (m, 1H), 3.01-3.06 (m, 1H),2.43-2.54 (m, 2H), 2.31-2.36 (m, 1H), 2.08-2.15 (m, 1H). $^{13}$C NMR (126 MHz, MeOD): δ 176.29, 174.56, 174.49, 162.39, 157.34, 137.24, 131.47, 128.69, 116.23, 55.52, 53.06, 37.96, 31.08, 28.26.

**GluTrp** yield 52% white powder. LCMS ESI$^+$: 494.15 [M+Na], expected mass for $C_{21}H_{21}N_5NaO_8^+$ 494.13. $^1$H NMR (500 MHz, MeOD): δ 7.71 (s, 1H), 7.55 (d, J=10.0 Hz, 1H), 7.29 (d, J=5.0Hz, 1H) 7.16 (s, 1H), 7.04 (t, J1=10.0 Hz, J2=5.0 Hz), 6.94 (t, J1=10.0 Hz, J2=5.0 Hz), 4.65 (t, J=5.0 Hz, 1H), 3.45-3.49 (m, 1H), 3.33-3.36 (m, 1H), 2.45-2.49 (m, 2H), 2.22-2.34 (m, 1H), 2.07-2.11 (m, 1H). $^{13}$C NMR (126 MHz, MeOD): δ 176.31, 174.88, 174.55, 137.96, 137.16, 128.80, 124.90, 122.32, 119.72, 119.31, 112.18, 110.52, 54.87, 53.03, 31.09, 30.05, 28.72, 28.26.

**GluArg** yield 60% white powder. LCMS ESI$^+$: 442.19 [M+H], expected mass for $C_{16}H_{24}N_7O_8^+$ 442.17. $^1$H NMR (500 MHz, MeOD): δ 7.79 (s, 1H), 4.63-4.69 (m, 2H), 3.23-3.28 (m, 2H), 2.45-2.50 (m, 2H), 2.30-2.33 (m, 1H), 2.03-2.15 (m, 2H), 1.90-1.94 (m, 1H) 1.71-1.78 (m, 2H). $^{13}$C NMR (126 MHz, MeOD): δ 176.3, 174.6, 174.5, 162.6, 158.6, 137.4, 128.7, 114.4, 55.9, 53.2, 53.1, 41.9, 31.1, 30.1, 28.2, 26.2.

**GluLys** yield 47% white powder. LCMS ESI$^+$: 436.16 [M+Na], expected mass for $C_{16}H_{23}N_5NaO_8^+$ 436.14. $^1$H NMR (500 MHz, MeOD): δ 7.78 (s, 1H), 4.66-4.69 (m, 1H), 4.61-4.63 (m, 1H), 2.97 (t, *J*=10.0 Hz, 2H), 2.46-2.49 (m, 2H), 2.30-2.34 (m, 1H), 2.09-2.14 (m, 1H), 2.00-2.04 (m, 1H), 1.91-1.95 (m, 1H), 1.71-1.74 (m, 1H). $^{13}$C NMR (126 MHz, MeOD): δ. 176.3, 174.8, 161.5, 137.4, 53.4, 53.0, 40.5, 32.3, 31.1, 28.2, 28.1, 23.6.

**GluLeu** yield 64% white powder. LCMS ESI$^+$: 421.16 [M+Na], expected mass for $C_{16}H_{22}N_4NaO_8^+$ 421.13. $^1$H NMR (500 MHz, MeOD): δ. 7.77 (s, 1H), 4.67 (t, J=5.0 Hz, 1H), 4.63 (t, J=5.0 Hz, 1H), 2.42-2.53 (m, 2H), 2.30-2.35 (m, 1H), 2.08-2.15 (m, 1H), 0.99 (d, J=5.0 Hz, 3H), 0.97 (d, J=5.0 Hz, 3H). $^{13}$C NMR (126 MHz, MeOD): δ. 176.2, 175.8, 174.6, 137.3, 137.2, 53.1, 52.3, 42.0, 31.1, 28.3, 26.2, 23.4, 22.0.

**GluThr** yield 58% white powder. LCMS ESI$^+$: 409.12 [M+Na], expected mass for $C_{14}H_{18}N_4NaO_9^+$ 409.10. $^1$H NMR (500 MHz, MeOD): δ 7.85 (s, 1H), 4.67-4.69 (m, 1H), 4.62 (d, J=5.0 Hz, 1H), 4.42-4.45 (m, 1H), 2.45-2.50 (m, 2H), 2.29-2.33 (m, 1H), 2.09-2.13 (m, 1H), 1.26 (d, J=5.0 Hz, 3H). $^{13}$C NMR (126 MHz, MeOD): δ176.2, 174.6, 173.6, 163.4, 161.7, 137.3, 132.5, 131.1, 68.6, 59.3, 53.1, 31.0, 28.2, 20.5.

**GluEa** yield 46% white powder. LCMS ESI$^+$: 329.14 [M+H], expected mass for $C_{12}H_{17}N_4O_7^+$ 329.11. $^1$H NMR (500 MHz, MeOD): δ 7.77 (s, 1H), 4.66 (s, 1H), 3.72 (s, 2H), 3.53 (s, 2H), 2.44-2.52 (m, 2H), 2.26-2.31 (m, 1H), 2.11-2.16 (m, 1H). $^{13}$C NMR (126 MHz, MeOD): δ 174.8, 173.3, 135.7, 131.5, 129.7, 121.7, 60.2, 51.7, 41.5, 29.7, 26.8

To a dry round-bottom flask **acyl chloride 1** (0.623 g, 2.0 mmol) was added followed by 10 mL of DCM and phenol (0.395 g, 4.2 mmol) under N$_2$. The suspension was cooled to 0 °C, and 320 μL of pyridine (4.0 mmol) was added dropwise. After 1 h, the solid was collected by vacuum filtration and washed with two 10 mL portions of DCM. The crude was purified by refluxing in DCM (30 mL), cooling to room temperature, and collecting the solid by filtration to yielded **Diphenyl ester**. **Diphenyl ester** (214 mg, 0.5 mmol) and 5 mL THF were added to a dry flask. **Tyrosine-OtBu** (237.0 mg, 1.0 mmol) and DIPEA were added to this suspension at 0 °C. After stirring at room temperature for 2 h, the reaction was refluxed for 2-4 days, monitored by TLC. The solvent was removed under vacuum and the tert-butyl protected intermediate was obtained by flash column chromatography. Then, this intermediate was dissolved in 5 mL TFA/DCM (1/1) for 2 h at room temperature. After all of the solvent was removed under vacuum, **diTyr** was purified by HPLC. Compounds **diTrp**, **diHis**, **diAp**, **diEa** and **diPEG** were synthesized using similar procedures (Scheme 2).

**diTyr** yield 41% as white powder. LCMS ESI$^+$: 505.15 [M+Na], expected mass for $C_{23}H_{22}N_4NaO_8$+ 505.13. $^1$H NMR (500 MHz, MeOD): δ 7.80 (s, 1H), 7.06 (d, J=10.0Hz, 4H), 6.67 (d, J=5.0Hz, 4H), 4.28 (t, J=5.0Hz, 2H), 3.21-3.24 (m, 2H), 3.03-3.07 (m, 2H). $^{13}$C NMR (126 MHz, MeOD): 174.4, 162.1, 157.3, 137.2, 131.5, 128.7, 116.2, 55.5, 37.9.

**diTrp** yield 42% as white powder. LCMS ESI$^+$: 529.20[M+H], expected mass for $C_{27}H_{25}N_6O_6^+$ 529.18. $^1$H NMR (500 MHz, MeOD): δ 8.12 (s, 1H), 7.07 (d, J=8.0 Hz, 2H), 7.12 (d, J=8.0 Hz, 2H), 6.96 (s, 2H), 6.86 (t, J=7.5 Hz, 2H), 6.75 (t, J=7.5 Hz, 2H), 4.76 (t, J=6.0 Hz, 2H), 3.30 (q, J=6.0 Hz, 2H), 3.17 (q, J=6.0 Hz, 2H); $^{13}$C NMR (126 MHz, MeOD): δ 173.28, 158.72, 136.56, 135.24, 128.77, 127.39, 123.53, 121.07, 118.46, 117.90, 110.95, 109.08, 53.93, 27.16.

**diHis** yield 30% as white powder. LCMS ESI$^+$: 453.16 [M+H], expected mass for $C_{17}H_{18}N_8NaO_6^+$ 453.12. $^1$H NMR (500 MHz, D$_2$O): δ 8.53 (s, 2H), 7.87 (s, 1H), 7.25

(s, 2H), 4.83 (t, $J$=6.0 Hz, 2H), 3.34 (dq, $J$1=6.0 Hz, $J$2=15.0 Hz, 4H); $^{13}$C NMR (126 MHz, D$_2$O): δ 173.87, 162.34, 138.14, 134.29, 130.91, 129.44, 118.27, 53.80, 27.88.

**diAp** yield as white powder. LCMS ESI$^+$: 303.20 [M+H], expected mass for C$_{11}$H$_{19}$N$_4$O$_6^+$ 303.13. $^1$H NMR (500 MHz, MeOD): δ 7.72 (s, 1H), 3.82 (t, $J$=5.0 Hz, 2H), 3.56-3.62 (m, 6H), 3.39-3.43 (dd, $J_1$=5.0 Hz, $J_2$=10.0 Hz, 2H). $^{13}$C NMR (126 MHz, MeOD): δ 161.9, 135.7, 130.7,70.6, 63.7, 41.9.

**diEa** yield as white powder. LCMS ESI$^+$: 241.91 [M-H], expected mass for C$_9$H$_{13}$N$_4$O$_4^-$ 241.09. $^1$H NMR (500 MHz, MeOD): δ 7.71 (s, 1H), 3.71 (t, $J$=5.0 Hz, 4H), 3.52 (t, $J$=5.0 Hz, 4H). $^{13}$C NMR (126 MHz, MeOD): δ 160.7, 137.0, 134.7, 61.6, 43.0, 42.7.

**diPEG** yield 35% as clear oil. LCMS ESI$^+$: 445.20 [M+H], expected mass for C$_{19}$H$_{33}$N$_4$O$_8^-$ 447.24. $^1$H NMR (500 MHz, MeOD): δ 7.63 (s, 1H), 3.65-3.68 (m, 14H), 3.55 (s, 4H), 3.38 (s, 6H). $^{13}$C NMR (75 MHz, CDCl$_3$): δ 163.6, 159.3, 135.23, 133.5, 128.3, 71.9, 70.6, 70.4, 69.7, 69.6, 59.0, 59.0, 39.5, 39.2.

To a stirring solution of **I45DCA** (312 mg, 2.0 mmol) in MeOH (20 mL) was added concentrated H$_2$SO$_4$ (2.0 mL). After refluxing for 6 h, the mixture was neutralized and extracted with ethyl acetate. Combined organic phase was dried over anhydrous Na$_2$SO$_4$, concentrated to give **I45DCE. I45DCE** was dissolved in MeOH (20 mL) and ethylenediamine (5 mL). The mixture was refluxed for 48 h. Then the solvent was evaporated and the residue purified by HPLC to get **diEda** (Scheme 3).

**diEda** yield 79%. LCMS ESI$^+$: 263.15 [M+Na], expected mass for C$_9$H$_{16}$N$_6$NaO$_2^+$ 263.12. $^1$H NMR (500 MHz, MeOD): δ 7.71 (s, 1H), 3.47 (t, $J$=5.0 Hz, 4H), 2.85 (t, $J$=5.0 Hz, 4H). $^{13}$C NMR (126 MHz, MeOD): δ 163.4, 137.3, 132.2, 42.9, 42.0.

## 2.3 Phantom studies

25 mM of **I45DCs** were dissolved in 0.01 M phosphate-buffered saline (PBS) and titrated using high concentrations of NaOH/HCl to produce 0.15 ml solutions with pH values of 4.5, 5.0, 5.6, 6.0, 6.2, 6.5, 6.9, and 7.4. The samples were kept at 37°C during imaging. CEST data were acquired on 9.4 T and 11.7 T vertical bore Bruker Avance systems using a RARE imaging sequence (TR/TE = 10000/5.58 ms, RARE factor = 32, FOV = 17 × 17 mm$^2$, slice 1.5 mm, matrix size = 64 × 64, spatial resolution = 0.27 × 0.27 mm$^2$) including a continuous-wave saturation pulse of 4 sec and six different saturation powers (B$_1$) of 2.4, 3.6, 4.8, 6.0, 8.4 and 10.2 μT. The CEST-weighted (M$_z$) images were collected at ninety-one frequency offsets between −13.5 ppm (−5400 Hz) and 13.5 ppm (5400 Hz) plus 1 at 20 000 Hz (M$_0$) to generate Z-spectra.

## 2.4 Calculation of exchange rates

The multiple saturation power **I45DC** Z-spectra for each pH were fit to numerical Bloch-McConnell solutions individually, using an open-source Matlab-based software (https://github.com/cest-sources/multiB1_fit_Z-cw_2pool)[8]. The Bloch-McConnell system consisted of either three or four pools, including ring NH protons (pool E, ω ~ 7.7 ppm), amide, amine and hydroxyl protons (pool D, ω ~ 2-4.5 ppm; pool B, ω = 1.5 ppm) and

water protons (pool A, $\omega = 0$ ppm). For the **I45DC-diEda**, an amide proton pool (pool E, $\omega \sim 5.0$ ppm) instead of the ring NH proton pool was simulated. The RARE readout was emulated by assuming the initial magnetization before the subsequent saturation phase to be small: $M_i = 0.1 \times M_0$. The longitudinal ($R_1$) and transverse ($R_2$) relaxation rates were fixed to: $R_{1A} = 0.25$ $s^{-1}$, $R_{1B} = R_{1D} = R_{1E} = 1$ $s^{-1}$, and $R_{2B} = R_{2D} = R_{2E} = 66.66$ $s^{-1}$, whereas the exchange rates ($k_{BA}$, $k_{DA}$, $k_{EA}$), relative concentrations ($f_{BA}$, $f_{DA}$, $f_{EA}$), and transverse relaxation of water, $R_{2A}$, were fit.

## 2.5 In vitro MR data post-processing and pH calculation

All post-processing was performed using in-house developed Matlab (version 2020b, MathWorks, USA) scripts. Briefly, the Z-spectra were interpolated on a voxel-by-voxel basis using smoothing splines, corrected for $B_0$ inhomogeneity, and saturation transfer (ST) value, $ST = 1 - M_z/M_0$, was measured. To generate a pH calibration curve, a region-of-interest (ROI)-based mean ST ratio $= (1-ST_{\delta1}) \times ST_{\delta2}/((1-ST_{\delta2}) \times ST_{\delta1})$ [30] was plotted as a function of titrated pH and fit to a $3^{rd}$ degree polynomial with $\delta_1 = 2.0, 3.0, 3.5$ or $4.5$ ppm and $\delta_2 = 5.0$ or $7.7$ ppm corresponding to the frequency offsets of two CEST signal regions. We used a $3^{rd}$ degree polynomial function to fit our data because the fit quality as measured by R-squared was higher than when a linear function or a $2^{nd}$ degree polynomial function was used. Using this pH correlation function, the pH values for all pixels showing a ST% effect higher than 15% of the maximum CEST contrast detected at frequency offsets $\delta_1$ or $\delta_2$ were calculated. To provide a quantitative measure that reflects the sensitivity of the investigated compounds to pH, the slope of a line connecting the two extreme points of the calibration curve (at highest and lowest pH) were obtained as: slope = arctan ($\Delta$pH/$\Delta$ST) and listed in Table 1. The range in detected pH values was determined by plotting the MRI pH measurements compared to that of electrode pH and selecting the linear region. Error bars were obtained by calculating the SD in pH over a single ROI enclosing the entire tube in the phantom at the respective pH.

## 2.6 In vitro cellular cytotoxicity assay

The release of lactate dehydrogenase (LDH) from cells serves as an indicator of cell death. A commercial LDH toxicity assay kit (Abcam Cat. # ab65393, USA) was used according to the manufacturer's specification to determine the toxicity of the compounds in a variant of Human Embryonic Kidney (HEK293T) cell line. Briefly, released LDH in culture supernatants of HEK 293T cells after 24 h co-culture with different concentration of Iopamidol, diGlu and diEda was measured as the indicator of lysed cells. The percentage of cytotoxicity was measured by subtracting LDH content in remaining viable cells from total LDH in untreated controls. The final absorbance was measured at 450 nm. All experiments were performed in triplicate.

## 2.7 Unilateral Urinary Obstruction mouse model

C57BL/6 mice were anesthetized with ~3% isoflurane, and the incision site infiltrated with 25 mL 0.25% bupivicaine. The anesthetized animal was placed in ventral recumbency with tail towards surgeon and a midline incision was made and kidney and bladder dissected and identified. The left ureter was suture ligated utilizing a 6-0 silk suture.

### 2.8 In vivo MRI measurements

All experiments conducted with mice were performed in accordance with protocols approved by the Johns Hopkins University Institutional Animal Care and Use Committee (IACUC). Mice were anesthetized prior to infusion of 100 µl of **I45DC-DiGlu** at a concentration of 300 mM. The animals were then positioned in an 11.7 T horizontal bore Bruker Biospec scanner (Bruker Biosciences, Billerica, MA) and were under isoflurane anesthesia for the entire image collection period. High resolution $T_{2W}$ images were acquired using a RARE sequence. To produce the CEST images, two sets of saturation images were collected, a WASSR set for $B_0$ mapping and a CEST data set for characterizing contrast. For the WASSR images, the saturation parameters were adjusted to stronger than normal to ensure water signal nulling in the presence of motion, $t_{sat}$ = 2100 msec, $B_1$ = 1.2 µT, TE/TR = 3.55/6670 msec with saturation offset incremented from −1.5 to +1.5 ppm with respect to water in 0.1 ppm steps. For the CEST images, these were acquired using a RARE sequence with centric encoding (saturation length = 2100 msec at $B_1$ = 6 µT) and RARE = 32 on a Bruker 11.7 T horizontal scanner. Other parameters were: TR/TE = 11000/3.55 ms, Matrix size = 64×64 and axial slice thickness = 1.5 mm, FOV = $29 \times 29$ mm$^2$. A two offset CEST protocol was used with offsets of 7.7 ppm and 4.5 ppm repeatedly up to 1 h 16 min after I45DCs administration. We collected 8-10 pre-injection and 100 post-injection images at the two frequency offsets. For *in vivo* pH mapping, post-injection ST maps at 4.5 ppm and 7.7 ppm were calculated from 26 images acquired at the peak enhancement time. Averaged pre-injection ST maps were then substracted from the post-injection ST maps to eliminate the endogenous CEST signals. The pH maps were calculated using the ST ratio and a pH calibartion curve obtained from the *in vitro* experiments.

## 3  RESULTS AND DISCUSSION

In this study, we synthesized a series of 14 new **I45DC** compounds. We previously identified **I45DC-diGlu** as a extracellular pH (pHe) imaging agent, and as shown in Table 1, the Z-spectra of **I45DC-diGlu** are suited for measuring pH values between 5.6 and 6.9 with a ring NH $k_{BA}$ ~ 5,081 s$^{-1}$ at pH 6.5, a typical pH for kidney tissue from CEST imaging measurements[30]. We were interested in producing a series of pHe probes with reduced overall formal charge than diGlu which will in turn reduce the osmolarity of the contrast media, that still possessed two labile proton signals suitable for ratiometric measurement of pH values from at least 5.6 – 7.0 with suitable labile protons exchange rates ($k_{BA}$, $k_{CA}$) falling between 300 – 8,000 s$^{-1}$ based on our previous simulations for optimizing 3 T detection[23]. We first prepared a series using amino acids with aliphatic sidechains, selecting the amino acid sidechains based on their potential for adjusting the intramolecular hydrogen bonding or slowing proton exchange and also to increase the formal charge of the compound[31]. We retained $R_4$ as glutamate and tested asymmetric substitutions with Fig. 1 showing their structures and Table 1 listing the CEST properties of these agents. The frequency offset and pH dependence of the second CEST signal varied among agents tested, and as a result, ratiometric CEST analysis provided slightly different pH detection ranges. Addition of weak electron acceptor groups led to narrower ranges of pH detection. We display the Z-spectra, pH calibration curves and pH maps for the best two in terms of ring NH $k_{BA}$ (GluLys, GluArg,) in Fig. 2b,c. While the $k_{BA}$ at pH 6.5 is better suited for CEST

contrast than diGlu and their formal charge is lower as well, they displayed a very small change in $ST_{ratio}$ over the range of physiological pH values with slopes of 85 ± and 79± respectively (Table 1) resulting in reduced quality pH maps (Fig. 2b,c far right panel). The guanidyl group and amino group can neutralize the charge of GluLys and GluArg, which also weakens the intramolecular hydrogen bonding of the ring NH through intermolecular hydrogen bonding and influencing the contrast efficiency. GluLeu and GluEa showed similar properties to GluArg so these are not displayed in Fig 2.

In order to test whether bulkier sidechains might increase the protection factor of the ring NH and thus reduce $k_{BA}$ further than the aliphatic variants, we prepared a series of anionic **I45DC** pH sensors with aromatic sidechain amino acids to determine how steric hindrance would influence CEST contrast. Of these, diHis did not possess ring NH protons suitable for detection. The unshared electron pair of the ring NH in imidazole easily leaves in the form of hydrogen ions, which can interact with the carbonyl group on $R_5$ position, leading to the quench of CEST signal. However, the CEST signal of diTrp is not influenced by the indole ring NHs. And the best (**diTrp**) is shown in Fig. 2d. While the formal charge is reduced, the $k_{BA}$ is suitable at pH 6.5 and slope of $ST_{ratio}$ vs pH suitable as well, the detectable pH range for this sensor is limited to pH values between 5.0 and 6.2 which also renders GluTrp, diTyr and GluTyr as reduced performance pH sensors. GluThr also performed similarly and as a result is not shown in Fig. 2. In addition, diTrp will aggregate in water below pH 6, which may be caused by the π -π stacking effect.

Based on these observations, we were interested in attaching basic and neutral substituents to this scaffold to determine if cationic or nonionic **I45DC** pH sensors would alter the detectable pH range of the I45DC sensors. Specifically, to get nonionic **I45DCs**, triethylene glycol monomethyl ether (PEG), 3-amino-1,2-propanediol (Ap) and ethanolamine (Ea) were conjugated and for cationic **I45DC** ethylenediamine (Eda) was conjugated (Figs. 1 & 2, Table 1). All these materials are very inexpensive and usually used as fragments of drugs. While nonionic diEa and diPEG displayed contrast at 7.7 ppm with a $k_{BA}$ closer to the optimal ~ 1,000 s$^{-1}$ which should enhance their 3 T contrast, the detectable pH range was significantly reduced. The nonionic diAp also displayed contrast at 7.7 ppm (Fig 3b), although $k_{BA}$ was too fast (> 9,000 s$^{-1}$ ) to be suitable for detection on 3 T clinical scanners. Based on these observations, we hypothesize that the lack of titratable groups on the nonionic derivatives resulted in the smaller range in detectable pH values. The Z-spectrum of cationic **I45DC-diEda** showed two distinct and relatively large peaks at 3.0 and 5.0 ppm instead, which originate from free amine proton groups on the side chains and ring NH on imidazole, respectively. In addition, diEda had the best $k_{BA}$ (381 s$^{-1}$) for detection at clinical field strengths and largest detectable pH range (4,5 – 7.4, Fig 3a) as well. We postulate this smaller chemical shift of 5.0 ppm is due to weakening of the intramolecular hydrogen bonding between the $R_5$ carbonyl group and ring NH on imidazole from the terminal cationic amino groups, leading to a smaller chemical shift from bulk water. Based on preferring agents with large detectable pH ranges while restricting kBA, kCA to be less than 8,000 s$^{-1}$, we performed HEK293 cell toxicity studies on diGlu and diEda (Fig. 4). As can be seen, **I45DC-diEda** displays a higher toxicity at 5 mM, 10 mM, 20 mM and 40 mM concentrations compared to **I45DC-diGlu** and iopamidol which are well

tolerated by these cells using these concentrations. Based on this, we selected **I45DC-diGlu** for further live animal testing.

We then proceeded to test the performance of our **I45DC-diGlu** analog for CEST imaging in a complete Unilateral Ureter Obstruction (UUO) mouse model of UTOs. In this model, markedly lower renal uptake of $^{99m}$Tc-MAG3 was observed 1 day after suture ligation[32] and histology showed tubular atrophy with interstitial fibrosis after 3 days[33]. We administered this compound and acquired CEST MRI data on a single slice containing the center of both kidneys using two offsets, 4.5 and 7.7 ppm to characterize how the contrast varied in time after injection. As shown in Fig. 5, the CEST contrast in the unobstructed kidney peaked at a time of around 180 – 300 sec whereas for the UUO kidney this contrast persisted out to 17 min, which is similar to what has been seen in a renal scintigraphy study on a mouse model of UUO by Tantawy et al[37]. In addition, the contrast is more uniform with larger ST values in the unobstructed kidney as seen in Fig 5A. We also produced pHe maps based on ratiometric contrast (Fig. 5B,D) and display histograms of pHe values across all pixels in each kidney (Fig. 5C,E) for n= 2 mice. These showed differences between the kidneys with the unobstructed kidney having relatively homogeneous pH values around 6.86±0.01 (Fig. 5B,C), while UUO kidneys showed an elevated pH of 6.97±0.01 and increased range in pHe values and the data being consistent between these mice. Based on our data, we concluded that **I45DC-diGlu** can depict differences in perfusion and pHe between unobstructed and UUO kidneys.

In the present study, we have synthesized 15 **I45DC** compounds with 14 new and 13 of these possessing far shifted labile protons resonating at 7.7 – 7.8 ppm from water and 1 (**I45DC-diEda**) with a labile proton 5 ppm from water. Inspiration for the compounds studied here was derived from the catalytic site of serine proteases. Such proteases have a well defined hydrogen bonding network, which slows the exchange of the imidazole N-H groups in histidine sufficiently to allow detection through CEST contrast, with the exchangeable proton demonstrating chemical shifts as far as 13 ppm downfield from water[34,35]. We were interested in maximizing the performance of the **I45DC** scaffold through testing a variety of substituents at the $R_4$ and $R_5$ positions and also testing whether symmetric and asymmetric substitutions would optimize the CEST properties for concentration independent measurement of pHe. The 14 **I45DCs** displaying strong contrast included anionic, cationic and nonionic compounds which show the versatility of this CEST imaging scaffold. Although, there is intramolecular hydrogen bonding for compounds of the I45DC class as described previously, the CEST contrast is pH and concentration dependent similar to CEST agents that don't display intramolecular bonding. Furthermore, these 14 compounds have at least two CEST active protons with different pH dependencies which enables generation of pHe maps using the ratio of these two signals, although the inflection points for signal ratio vs pHe is not ideal for some to measure pHe over the entire physiologically relevant range. Compared to the triiodobenzene CEST pHe imaging agents including iopamidol and iopromide which have a significant advantage of FDA approval, the main labile protons are an additional 2 ppm further shifted from water, which should allow better discrimination from background tissue. In addition, the exchange rates are faster in general and therefore larger saturation $B_1$'s should be applied to detect these **I45DC** CEST agents. In summary,

our phantom CEST experiments showed that a wide range of pHe values could be measured using these **I45DC** probes.

Furthermore, we demonstrate successful detection of our frontline compound (**I45DC-diGlu**) in a mouse model of UTO with clear differences in contrast kinetics and pHe maps seen using this agent. Specifically, we observed an elevated pHe for the UUO kidney. Our findings can be contextualized in the observations of previous studies, which demonstrated increased pHe values after glycerol-induced injury[36], after unilateral ischemia-reperfusion injury[37] and also after UUO when using iopamidol as a pH sensor [38]. Impaired urinary acidification has also been documented in patients with various types of obstructive nephropathy[39]. One issue with using iodinated contrast agents is that contrast induced nephropathy is a known risk factor. Our **I45DCs** are similar to flumizole, dacarbazine and cimetidine and a number of other drugs which have LD50s of 500 –2,500 mg/kg and are used as antiinflammatories, anticancer, $H_2$ antagonists and others[40,41]. Based on this similarity and our cell toxicity results, we expect that **I45DC-diGlu** and other **I45DCs** should be well tolerated.

A limitation of using CEST agents for ratiometric based pH imaging is the need to have sufficient signal intensity for both labile protons across all pH values to allow for precise pH measurements. By analyzing the CEST efficiency of our new **I45DCs** CEST agents, we suspect that intermolecular hydrogen bonding, intramolecular hydrogen bonding, molecular charge and π-π stacking effects are the main factors that influence the signal intensity as a function of pH. While we have not identified an ideal agent across all pH values of physiological interest, **I45DC-diGlu** can measure a fairly wide range of pH values and the other **I45DCs** agents synthesized and tested may provide ideas on designing more efficient diaCEST contrast agents in the future.

## 4  CONCLUSIONS

We have synthesized 14 imidazoles which can be used as CEST imaging agents for depicting perfusion and pH changes. **I45DC-diGlu,** which to date displayed the best exchange properties for a compound with large labile proton chemical shift (7.7 ppm), was able to depict differences in contrast kinetics and pH values between obstructed and unobstructed kidneys in a mouse model of UTO. Overall, our results suggest that **I45DC** compounds are very promising CEST probes, particularly for measuring pH.

## Funding Sources

## Abbreviations

| | |
|---|---|
| **MRI** | magnetic resonance imaging |
| **CEST** | chemical exchange saturation transfer |
| **I45DC** | imidazole-4,5-dicarboxyamide |

| | |
|---|---|
| **Eda** | ethylenediamine |
| **Ap** | 3-amino-1,2-propanediol |
| **Ea** | ethanolamine |
| **UTO** | urinary tract obstruction |
| **UUO** | unilateral ureter obstruction |
| **SD** | standard deviation |
| **DMF** | N,N-Dimethylformamide |
| **TFA** | trifluoroacetic acid |
| **DCM** | dichloromethane |
| **THF** | tetrahydrofuran |
| **DIPEA** | diisopropylethylamine |
| **ESI** | electrospray ionization |
| **MeOD** | deuterated methanol |
| **ω** | chemical shift difference with water in ppm |
| **$k_{BA}$** | chemical exchange rate from pool B to pool A |
| **ST** | saturation transfer |
| **CKD** | chronic kidney disease |
| **AKI** | acute kidney injury |

## References:

1. Hancu I, Dixon WT, Woods M, Vinogradov E, Sherry AD, Lenkinski RE. CEST and PARACEST MR contrast agents. Research Support, N.I.H., Extramural Review. Acta Radiol. Oct 2010;51(8):910–23. doi:10.3109/02841851.2010.502126 [PubMed: 20828299]

2. van Zijl PC, Yadav NN. Chemical exchange saturation transfer (CEST): what is in a name and what isn't? Research Support, N.I.H., Extramural. Magnetic resonance in medicine : official journal of the Society of Magnetic Resonance in Medicine / Society of Magnetic Resonance in Medicine. Apr 2011;65(4):927–48. doi:10.1002/mrm.22761

3. Terreno E, Castelli DD, Aime S. Encoding the frequency dependence in MRI contrast media: the emerging class of CEST agents. Contrast Media and Molecular Imaging. Mar-Apr 2010;5(2):78–98. doi:10.1002/cmmi.369 [PubMed: 20419761]

4. Liu G, Song X, Chan KW, McMahon MT. Nuts and bolts of chemical exchange saturation transfer MRI. NMR Biomed. Jul 2013;26(7):810–28. doi:10.1002/nbm.2899 [PubMed: 23303716]

5. McMahon MT, Gilad AA, Bulte JWM, van Zijl PCM. Chemical Exchange Saturation Transfer Imaging: Advances and Applications. 1st ed. Pan Stanford Publishing; 2017:479.

6. Zaiss M, Bachert P. Chemical exchange saturation transfer (CEST) and MR Z-spectroscopy in vivo: a review of theoretical approaches and methods. Physics in medicine and biology. Nov 21 2013;58(22):R221–69. doi:10.1088/0031-9155/58/22/r221 [PubMed: 24201125]

7. Aime S, Barge A, Delli Castelli D, et al. Paramagnetic lanthanide(III) complexes as pH-sensitive chemical exchange saturation transfer (CEST) contrast agents for MRI applications. Magn Reson Med. Apr 2002;47(4):639–48. [PubMed: 11948724]

8. Zaiss M, Anemone A, Goerke S, et al. Quantification of hydroxyl exchange of D-Glucose at physiological conditions for optimization of glucoCEST MRI at 3, 7 and 9.4 Tesla. 10.1002/ nbm.4113. NMR in Biomedicine. 2019/09/01 2019;32(9):e4113. doi:10.1002/nbm.4113 [PubMed: 31313865]

9. Jones KM, Randtke EA, Yoshimaru ES, et al. Clinical Translation of Tumor Acidosis Measurements with AcidoCEST MRI. Molecular imaging and biology : MIB : the official publication of the Academy of Molecular Imaging. Aug 2017;19(4):617–625. doi:10.1007/s11307-016-1029-7

10. Zhang S, Seiler S, Wang X, et al. CEST-Dixon for human breast lesion characterization at 3 T: A preliminary study. 10.1002/mrm.27079. Magn Reson Med. 2018/09/01 2018;80(3):895–903. doi:10.1002/mrm.27079 [PubMed: 29322559]

11. Zhao X, Wen Z, Zhang G, et al. Three-Dimensional Turbo-Spin-Echo Amide Proton Transfer MR Imaging at 3-Tesla and Its Application to High-Grade Human Brain Tumors. Molecular Imaging and Biology. 2013/02/01 2013;15(1):114–122. doi:10.1007/s11307-012-0563-1 [PubMed: 22644987]

12. Xu X, Yadav NN, Knutsson L, et al. Dynamic glucose-enhanced (DGE) MRI: translation to human scanning and first results in glioma patients. Tomography. 2015;1(2):105–114. [PubMed: 26779568]

13. Schuenke P, Paech D, Koehler C, et al. Fast and Quantitative T1ρ-weighted Dynamic Glucose Enhanced MRI. Scientific Reports. 2017/02/07 2017;7(1):42093. doi:10.1038/srep42093 [PubMed: 28169369]

14. Yang J, Sun BG, Min H-J, et al. Impact of acute kidney injury on long-term adverse outcomes in obstructive uropathy. Scientific reports. 2021;11(1):1–9. [PubMed: 33414495]

15. Mishra J, Dent C, Tarabishi R, et al. Neutrophil gelatinase-associated lipocalin (NGAL) as a biomarker for acute renal injury after cardiac surgery. Lancet (London, England). Apr 2-8 2005;365(9466):1231–8. doi:10.1016/s0140-6736(05)74811-x [PubMed: 15811456]

16. Sarhan O, Helmy T, Abou-El Ghar M, Baky MA, El-Assmy A, Dawaba M. Long-term functional and morphological outcome after pyeloplasty for huge renal pelvis. BJU International. 2011/03/01 2011;107(5):829–833. doi:10.1111/j.1464-410X.2010.09566.x [PubMed: 20735380]

17. Carpenter CP, Tolley E, Tourville E, Sharadin C, Giel DW, Gleason JM. Hydronephrosis After Pyeloplasty: "Will It Go Away?". Urology. Nov 2018;121:158–163. doi:10.1016/ j.urology.2018.08.010 [PubMed: 30125645]

18. van Sluis R, Bhujwalla ZM, Raghunand N, et al. In vivo imaging of extracellular pH using (1)H MRSI. Article. Magn Reson Med. Apr 1999;41(4):743–750. [PubMed: 10332850]

19. Raghunand N, Howison C, Sherry AD, Zhang S, Gillies RJ. Renal and systemic pH imaging by contrast-enhanced MRI. Magn Reson Med. Feb 2003;49(2):249–57. doi:10.1002/mrm.10347 [PubMed: 12541244]

20. Raghunand N, Zhang S, Sherry AD, Gillies RJ. In vivo magnetic resonance imaging of tissue pH using a novel pH-sensitive contrast agent, GdDOTA-4AmP. Acad Radiol. Aug 2002;9 Suppl 2:S481–3. [PubMed: 12188315]

21. Gallagher FA, Kettunen MI, Day SE, et al. Magnetic resonance imaging of pH in vivo using hyperpolarized 13C-labelled bicarbonate. Nature. 2008/06/01 2008;453(7197):940–943. doi:10.1038/nature07017 [PubMed: 18509335]

22. Pollard AC, de la Cerda J, Schuler FW, et al. Radiometal-Based PET/MRI Contrast Agents for Sensing Tumor Extracellular pH. Biosensors. 2022;12(2):134. [PubMed: 35200394]

23. Yang X, Yadav NN, Song X, et al. Tuning Phenols with Intra-Molecular Bond Shifted HYdrogens (IM-SHY) as diaCEST MRI Contrast Agents. Chem Euro J. 2014;20(48):15824–15832.

24. Yang X, Song XL, Li YG, et al. Salicylic Acid and Analogues as diaCEST MRI Contrast Agents with Highly Shifted Exchangeable Proton Frequencies. Article. Angew Chem-Int Edit. Jul 2013;52(31):8116–8119. doi:10.1002/anie.201302764

25. Dang T, Suchy M, Truong YJ, et al. Hydrazo-CEST: Hydrazone-Dependent Chemical Exchange Saturation Transfer Magnetic Resonance Imaging Contrast Agents. Chemistry (Weinheim an der

Bergstrasse, Germany). Jun 26 2018;24(36):9148–9156. doi:10.1002/chem.201801671 [PubMed: 29645309]

26. Chakraborty S, Peruncheralathan S, Ghosh A. Paracetamol and other acetanilide analogs as inter-molecular hydrogen bonding assisted diamagnetic CEST MRI contrast agents. RSC Advances. 2021;11(12):6526–6534. [PubMed: 35423188]

27. Chakraborty S, Das M, Srinivasan A, Ghosh A. Tetrakis-(N-methyl-4-pyridinium)-porphyrin as a diamagnetic chemical exchange saturation transfer (diaCEST) MRI contrast agent. 10.1039/D0NJ04869K. New Journal of Chemistry. 2021;45(3):1262–1268. doi:10.1039/D0NJ04869K

28. Zhang X, Yuan Y, Li S, et al. Free-base porphyrins as CEST MRI contrast agents with highly upfield shifted labile protons. Magn Reson Med. Aug 2019;82(2):577–585. doi:10.1002/mrm.27753 [PubMed: 30968442]

29. Yang X, Song X, Ray Banerjee S, et al. Developing imidazoles as CEST MRI pH sensors. Contrast Media Mol Imaging. 2016;11(4):304–312. [PubMed: 27071959]

30. Longo DL, Dastru W, Digilio G, et al. Iopamidol as a Responsive MRI-Chemical Exchange Saturation Transfer Contrast Agent for pH Mapping of Kidneys: In Vivo Studies in Mice at 7 T. Article. Magn Reson Med. Jan 2011;65(1):202–211. doi:10.1002/mrm.22608 [PubMed: 20949634]

31. Bai Y, Milne JS, Mayne L, Englander SW. Primary Structure Effects on Peptide Group Hydrogen Exchange. PROTEINS. 1993;17:75–86. [PubMed: 8234246]

32. Tantawy MN, Jiang R, Wang F, et al. Assessment of renal function in mice with unilateral ureteral obstruction using 99mTc-MAG3 dynamic scintigraphy. BMC Nephrology. 2012/12/10 2012;13(1):168. doi:10.1186/1471-2369-13-168 [PubMed: 23228112]

33. Wang F, Takahashi K, Li H, et al. Assessment of unilateral ureter obstruction with multi-parametric MRI. 10.1002/mrm.26849. Magn Reson Med. 2018/04/01 2018;79(4):2216–2227. doi:10.1002/mrm.26849 [PubMed: 28736875]

34. Lauzon CB, van Zijl P, Stivers JT. Using the water signal to detect invisible exchanging protons in the catalytic triad of a serine protease. Article. J Biomol NMR. Aug 2011;50(4):299–314. doi:10.1007/s10858-011-9527-z [PubMed: 21809183]

35. Bachovchin WW. Contributions of NMR spectroscopy to the study of hydrogen bonds in serine protease active sites. Review. Magn Reson Chem. Dec 2001;39:S199–S213. doi:10.1002/mrc.951

36. Longo DL, Busato A, Lanzardo S, Antico F, Aime S. Imaging the pH evolution of an acute kidney injury model by means of iopamidol, a MRI-CEST pH-responsive contrast agent. Magn Reson Med. Sep 2013;70(3):859–64. doi:10.1002/mrm.24513 [PubMed: 23059893]

37. Longo DL, Cutrin JC, Michelotti F, Irrera P, Aime S. Noninvasive evaluation of renal pH homeostasis after ischemia reperfusion injury by CEST-MRI. Nmr in Biomedicine. Jul 2017;30(7)e3720. doi:10.1002/nbm.3720

38. Stabinska J, Singh A, Haney NM, et al. Noninvasive assessment of renal dynamics and pH in a unilateral ureter obstruction model using DCE MR-CEST urography. Magn Reson Med. 2023;89(1):343–355. doi:10.1002/mrm.29436 [PubMed: 36089805]

39. Chávez-Iñiguez JS, Navarro-Gallardo GJ, Medina-González R, Alcantar-Vallin L, García-García G. Acute kidney injury caused by obstructive nephropathy. International Journal of Nephrology. 2020;2020

40. K LT. Pharmacological activity and toxicity of neurotropic agents in experimental hypodynamia. Farmakol Toksikol. 1979;42(3):221–225. [PubMed: 446700]

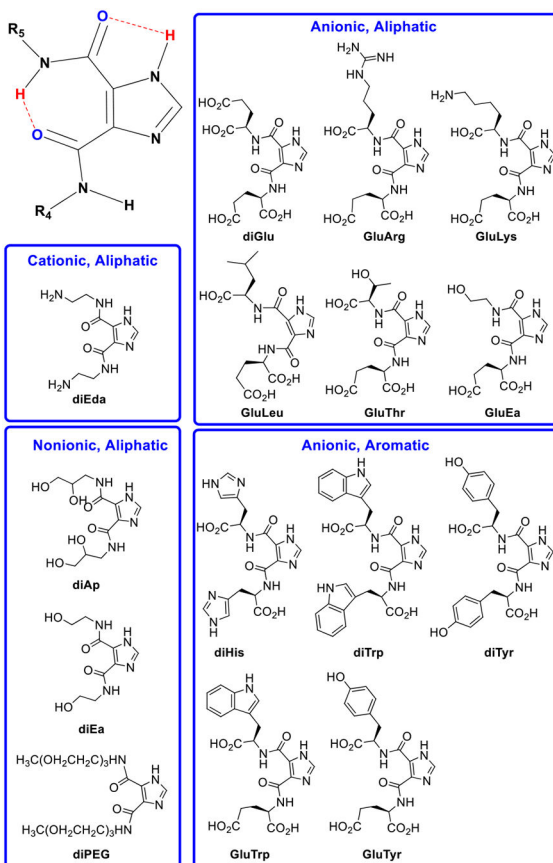41. Kniga M. Farmakol Toksikol. 1959;22:11. [PubMed: 13653118]

**Figure 1.**

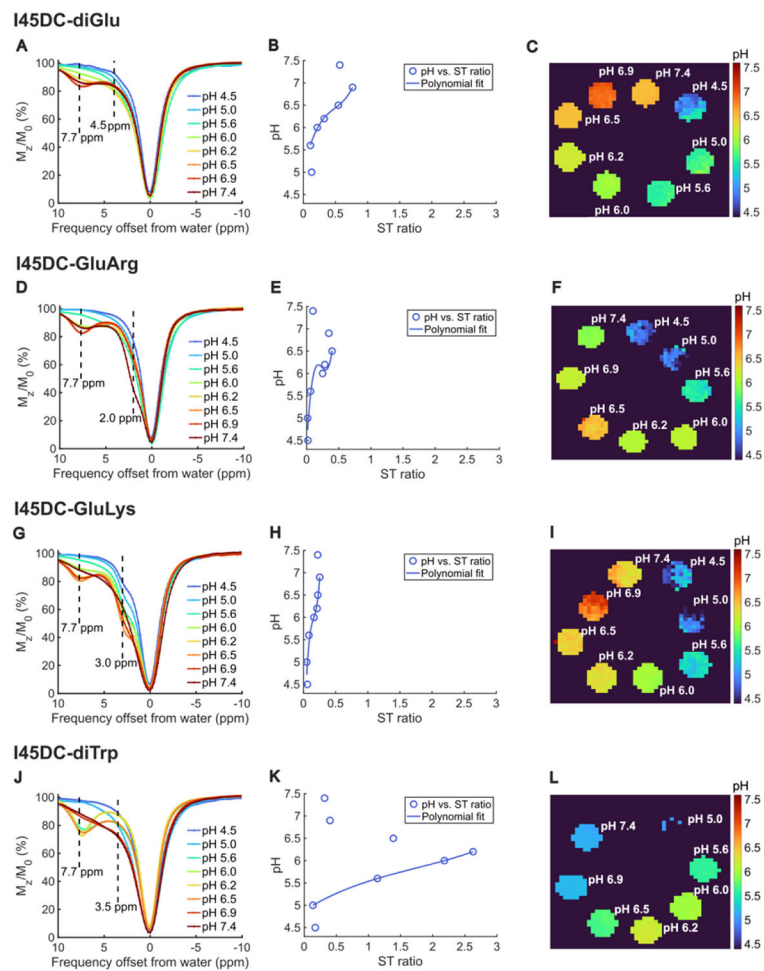Structure of **I45DC** scaffold and imaging agents synthesized and tested in this study.

**Figure 2.**
in vitro CEST Z-spectra, ST$_{ratio}$ vs pH and pH maps for anionic **I45DC** agents; A-C) **I45DC-diGlu**; D-F) **I45DC-GluArg**; G-I) **I45DC-GluLys**; J-L) **I45DC-diTrp**; Conditions: CEST data were obtained at 25 mM concentration, t$_{sat}$ = 4 sec and 37 ±C. Please note that some pH maps show values that are far from the titrated pH values which is due to the limited pH sensitivity range of the compounds.
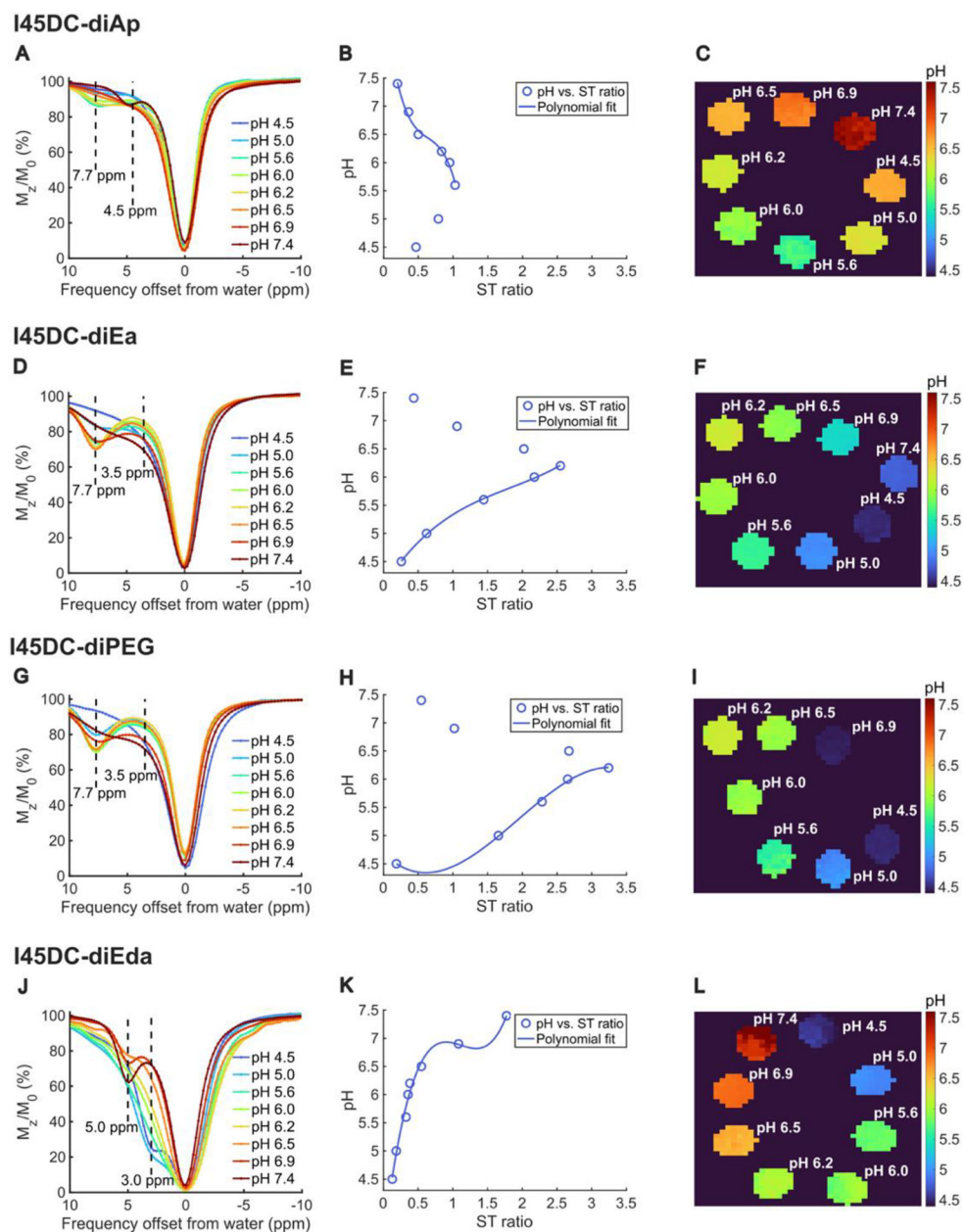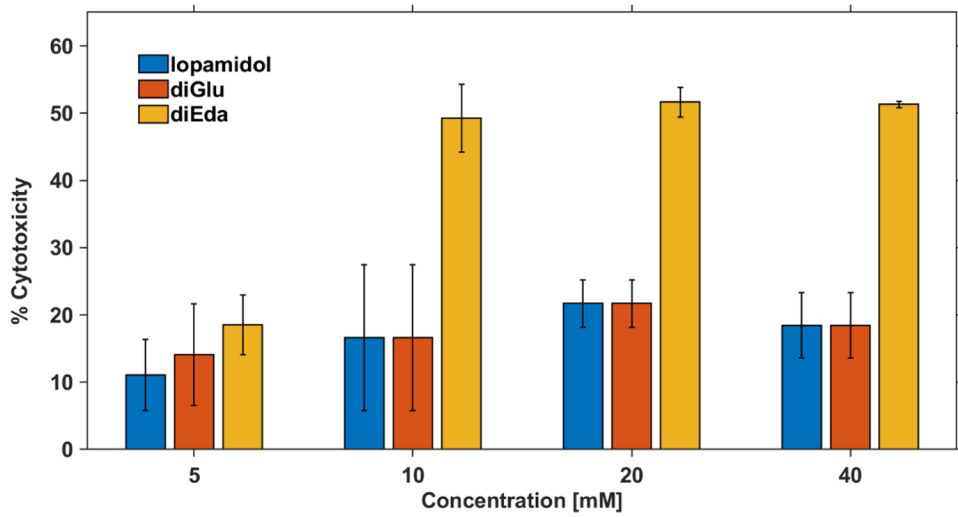
**Figure 3.**
in vitro CEST Z-spectra, $ST_{ratio}$ vs pH and pH maps for cationic and neutral **I45DC** agents; A) **I45DC-diEda**; B) **I45DC-diAp**; C) **I45DC-diEa**; D) **I45DC-diPEG**; Conditions: CEST data were obtained at 25 mM concentration, $t_{sat}$ = 4 sec and 37 ±C. Please note that some pH maps show values that are far from the titrated pH values which is due to the limited pH sensitivity range of the compounds.

**Figure 4.**
Cell Cytotoxicity of the three CEST pH imaging agents Iopamidol, I45DC-diGlu, I45DC-diEda. This was measured by incubating HEK293T cells with these agents.
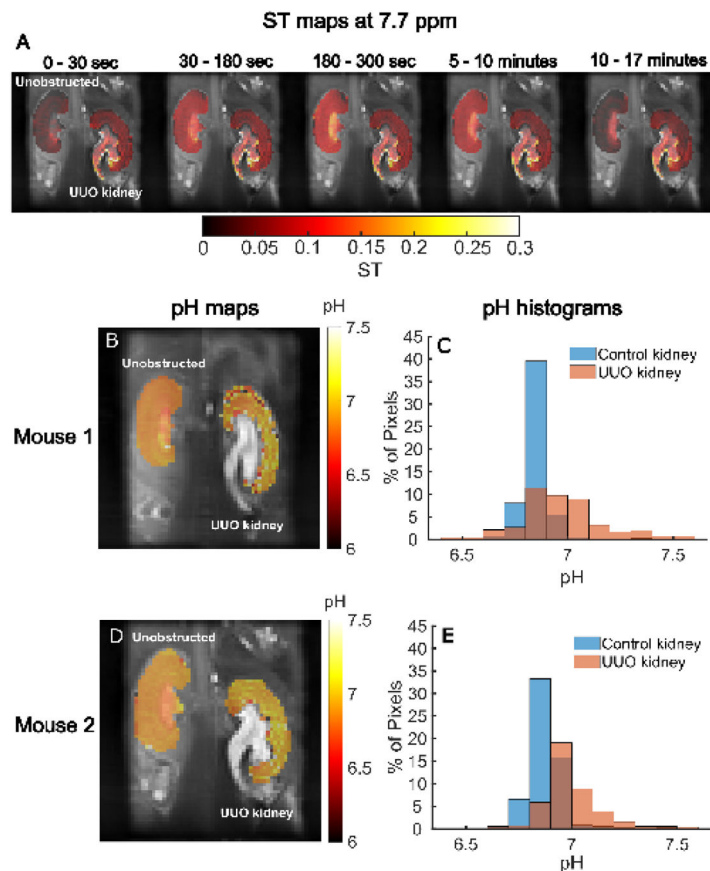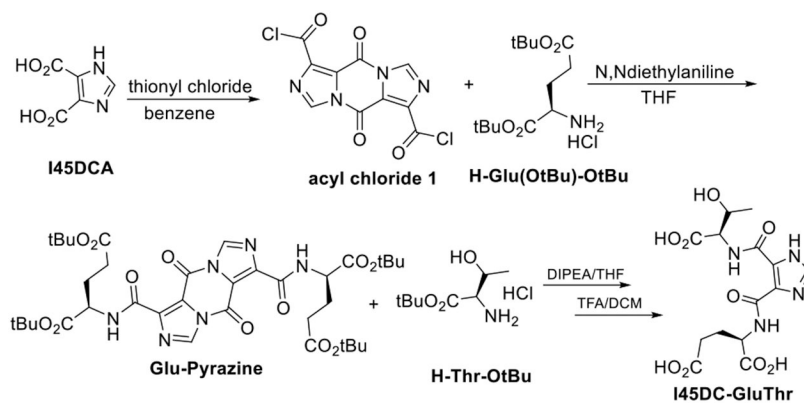
**Figure 5.**

In vivo CEST MRI of UUO mice for **I45DC-diGlu**; (**A**) ST maps at 7.7 ppm of a representative mouse calculated by averaging images acquired in different time ranges after administration of **I45DC-diGlu** overlayed on high resolution $T_{2W}$ anatomic images; pHe maps (B, D) and (C, E) pHe histograms of two UUO mice following **I45DC-diGlu** injection.

**Scheme 1.**
Synthesis for I45DC-GluThr.
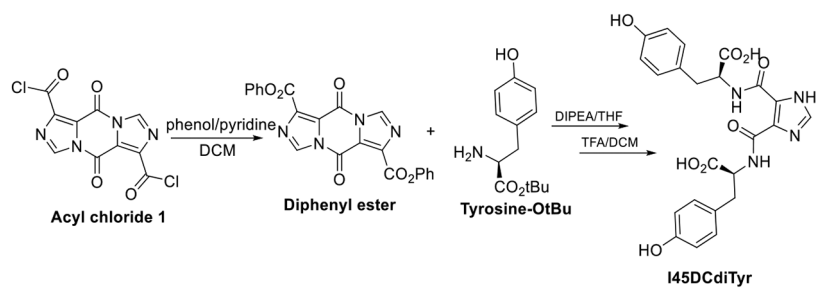
**Scheme 2.**
Synthesis of I45DCdiTyr.
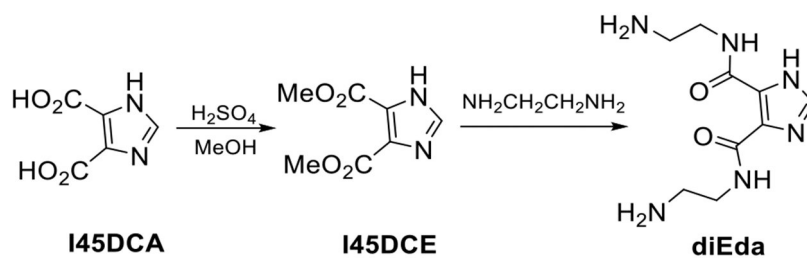
**Scheme 3.**
Synthesis of I45DC-diEda.

**Table 1.**

CEST properties of **I45DC** contrast agents synthesized

| Compound | Chemical shifts [$\delta_1$, $\delta_2$, ppm] | Detectable pH range | ST$_{ratio}$ slope (°) | K$_{BA}$ (s$^{-1}$) at 7.7 ppm pH 6.5 |
|---|---|---|---|---|
| *Anionic Aliphatic* | | | | |
| **I45DC-diGlu** | 4.5, 7.7 | 5.6 – 7.0 | 53 | 5,081 |
| **I45DC-GluLys** | 3.0, 7.7 | 4.5 – 7.0 | 85 | 3,413 |
| **I45DC-GluArg** | 2.0, 7.7 | 4.5 – 6.5 | 79 | 3,449 |
| **I45DC-GluThr** | 4.5, 7.7 | 5.6 – 6.5 | 33 | 2,140 |
| **I45DC-GluEa** | 2.0, 7.7 | 5.6 – 6.5 | 70 | 3,950 |
| **I45DC-GluLeu** | 2.0, 7.7 | 5.6 – 6.5 | 78 | 6,767 |
| *Anionic Aromatic* | | | | |
| **I45DC-diTrp** | 3.5, 7.7 | 5.0 – 6.2 | 26 | 3,416 |
| **I45DC-diTyr** | 3.0, 7.7 | 5.0 – 6.5 | 74 | 2,628 |
| **I45DC-diHis** * | - | - | - | - |
| **I45DC-GluTrp** | 3.5, 7.7 | 5.6 – 6.5 | 32 | 2,499 |
| **I45DC-GluTyr** | 3.0, 7.7 | 5.6 – 6.5 | 62 | 3,539 |
| *Cationic Aliphatic* | | | | |
| **I45DC-diEda** ** | 3.0, 5.0 | 4.5 – 7.4 | 60 | 381 |
| *Nonionic Aliphatic* | | | | |
| **I45DC-diAp** | 4.5, 7.7 | 5.6 – 7.4 | 65 | 9,442 |
| **I45DC-diEa** | 3.5, 7.7 | 6.2 – 7.4 | 30 | 2,745 |
| **I45DC-diPEG** | 3.5, 7.7 | 6.2 – 7.4 | 24 | 2,038 |

*
There is no peak at 7.7 ppm or 5 ppm observed.

**
Peak is at 5 ppm instead of 7.7 ppm. Conditions: CEST data were obtained at 25 mM concentration, $t_{sat}$ = 4 sec and 37 ±C.